

Article

The Influence of Oxygen Activity on Phase Composition, Crystal Structure, and Electrical Conductivity of $\text{CaV}_{1-x}\text{Mo}_x\text{O}_{3\pm\delta}$

Semyon A. Belyakov ^{1,*}, Evgeny Yu. Gerasimov ²  and Anton V. Kuzmin ³

¹ Laboratory of Electrochemical Materials Science, Institute of High-Temperature Electrochemistry UB RAS, 620137 Yekaterinburg, Russia

² Federal Research Center Boreskov Institute of Catalysis SB RAS, 630090 Novosibirsk, Russia; gerasimov@catalysis.ru

³ Department of Technology of Inorganic Materials and Electrochemical Production, Vyatka State University, 610000 Kirov, Russia; a.v.kuzmin@yandex.ru

* Correspondence: bca2@mail.ru

Abstract: Perovskite-like vanadate-molybdates are interesting from the point of view of their metal-like conductivity, which combines the correlated and free electron nature. A series of $\text{CaV}_{1-x}\text{Mo}_x\text{O}_{3-\delta}$ solid solutions was considered near the Mo concentration $x = 0.4$, where a difficult-to-perceive structural transition was previously detected. High-resolution transmission electron microscopy revealed the phase separation of $\text{CaV}_{0.6}\text{Mo}_{0.4}\text{O}_{3-\delta}$ into nanoscale regions with different ratios of V and Mo concentrations, despite X-ray diffraction analysis exhibiting a homogeneous perovskite structure. The rest of the compositions from the $\text{CaV}_{1-x}\text{Mo}_x\text{O}_{3-\delta}$ series do not show phase separation. The nonmonotonic behavior of the conductivity and linear expansion of $\text{CaV}_{1-x}\text{Mo}_x\text{O}_{3\pm\delta}$ was shown when the oxygen activity in the $\text{N}_2\text{-H}_2\text{-H}_2\text{O}$ gas mixture was varied, which is mainly determined by the partial decomposition of the perovskite phase. Against this background, the behavior of the electrical properties of the $\text{CaV}_{1-x}\text{Mo}_x\text{O}_{3\pm\delta}$ individual phase remains unclear.

Keywords: perovskite; vanadate; molybdate; metal-like conductivity; chemical expansion; phase separation



Citation: Belyakov, S.A.; Gerasimov, E.Y.; Kuzmin, A.V. The Influence of Oxygen Activity on Phase Composition, Crystal Structure, and Electrical Conductivity of $\text{CaV}_{1-x}\text{Mo}_x\text{O}_{3\pm\delta}$. *Crystals* **2022**, *12*, 419. <https://doi.org/10.3390/cryst12030419>

Academic Editor: Bo Chen

Received: 28 February 2022

Accepted: 16 March 2022

Published: 18 March 2022

Publisher's Note: MDPI stays neutral with regard to jurisdictional claims in published maps and institutional affiliations.



Copyright: © 2022 by the authors. Licensee MDPI, Basel, Switzerland. This article is an open access article distributed under the terms and conditions of the Creative Commons Attribution (CC BY) license (<https://creativecommons.org/licenses/by/4.0/>).

1. Introduction

Perovskite-like vanadates ($(\text{Ca,Sr})\text{VO}_3$) and molybdates ($(\text{Ca,Sr})\text{MoO}_3$) represent an interesting class of materials and are oxides with metal-like conductivity. Overlapping between neighboring d-orbitals of V or Mo through oxygen 2p-orbitals leads to a strong delocalization of electrons, which is a source of tunneling electron transfer [1,2]. Orthorhombic distortions of the crystal structure in CaVO_3 and CaMoO_3 reduce the Me–O–Me bond angle to 160° [3,4], relative to the ideal 180° in cubic SrVO_3 and SrMoO_3 , which is accompanied by a decrease in the orbital overlap integral and, therefore, leads to a decrease in the transfer electron bandwidth [1,5,6]. A similar phenomenon is observed for vanadate-molybdates ($(\text{Ca,Sr})\text{V}_{0.5}\text{Mo}_{0.5}\text{O}_3$) [7].

Vanadates are correlated metals, as they exhibit strong electron–electron interactions [2,8], which opens up a number of interesting uses. Vanadium oxides are considered as promising systems, and undergo a metal–insulator transition (Mott transition) [9] which makes their use in electronics possible, for example, in components of transistors or relaxation oscillators. However, the metal–insulator transition, although expected, was not previously observed in the bulk form of $(\text{Ca,Sr})\text{VO}_3$ [8,10]. It was shown that dimensional constraints, when in the form of thin films, and epitaxial deformation enhance the correlation effects, which brings these systems closer to the metal–insulator transition [11–13]. In addition, a new approach to the design of oxide transparent conductors is based on controlling the concentration and effective mass of delocalized electrons, in order to achieve high

conductivity and transparency in the visible region of the electromagnetic spectrum [10,14]. This allows metal-like oxides to be used as transparent electrodes in organic light-emitting diodes. Finally, high electronic conductivity combined with an oxygen transfer at high temperatures makes it possible to use partially substituted vanadates as a fuel electrode in electrochemical power sources [15–17], although their low thermodynamic stability at high temperatures remains a problem [18,19].

Molybdates, unlike vanadates, do not exhibit electron–electron scattering, and are similar in behavior to normal metals [1,20,21]. Their use as electrodes in electrochemical devices is limited due to their low redox stability [22,23], although with partial substitution of Mo for strontium ferrites, promising results can be obtained [24,25], but with a significant decrease in the conductivity of the electrode material.

The effect of oxygen nonstoichiometry (δ) on the structure and electronic properties of $\text{CaVO}_{3-\delta}$ was studied by Ueda et al. [26,27]. The initially detected transition from a metallic state to an insulator [28] was associated with a partial oxidation of the ceramic surface [26,29]. A small region of oxygen over-stoichiometry ($3 + \delta$) in $(\text{Ca,Sr})\text{VO}_{3\pm\delta}$ vanadates was shown [30,31], after which oxidation to the phases $(\text{Ca,Sr})_3\text{V}_2\text{O}_8$ and $(\text{Ca,Sr})_2\text{V}_2\text{O}_7$ was observed [15,16,30]. On the other hand, the use of highly reducing conditions for the synthesis of perovskite-like vanadates implies a large oxygen deficiency. In perovskite-like oxides, a transition to domainized brownmillerite-like structures is possible, as is well-known for strontium ferrite [32], although additions of V and Mo to strontium ferrite “smooth out” these transitions and reduce domain wall thickness [33–35]. The perovskite–brownmillerite transition may be preceded by the ordering of oxygen vacancies. Accordingly, Ueda et al. [26,27] showed the formation of oxygen vacancy channels for $\text{CaVO}_{3-\delta}$ at different values of oxygen nonstoichiometry. It should be taken into account that even small structural distortions have a large effect on the electronic structure of perovskite-like vanadates. The Fermi surface shape for CaVO_3 was investigated by Inoue et al. [36] in the form of an ideal model only, which does not reflect the effect of oxygen nonstoichiometry and the related distortions of the crystal structure of the material. The effect of oxygen activity (a_{O_2}) on the electronic structure of vanadates and molybdates has scarcely been studied. The significant influence of oxygen vacancies has been shown only on the electronic structure of vanadates [37], while in molybdates their influence is considered insignificant [21].

Perovskite-like vanadate–molybdates $(\text{Ca,Sr})(\text{V,Mo})\text{O}_{3-\delta}$ are interesting from the point of view of their electronic properties, as they combine the correlated electron nature of vanadates and the free electron nature of molybdates [38]. Unfortunately, the effect of oxygen activity on the properties of vanadate–molybdates has not yet been studied. Earlier, we presented information on the behavior of the electronic properties with temperature of $\text{CaV}_{1-x}\text{Mo}_x\text{O}_{3-\delta}$ ($0 \leq x \leq 0.6$) in a dry hydrogen atmosphere [38]. In addition, we were puzzled by the previously discovered transition region at the Mo concentration $x = 0.4$ [38,39], where some structurally related changes take place. In the current work, we examine in detail the structure and microstructure of powders and ceramics of $\text{CaV}_{1-x}\text{Mo}_x\text{O}_{3-\delta}$ ($0.3 \leq x \leq 0.5$), and evaluate the effect of oxygen activity on conductivity and chemical expansion.

2. Materials and Methods

The $\text{CaV}_{1-x}\text{Mo}_x\text{O}_{3-\delta}$ ($0.3 \leq x \leq 0.5$) powders were prepared via pyrolysis of formate solutions according to the technique from [40]. Stoichiometric quantities of CaCO_3 , NH_4VO_3 and $(\text{NH}_4)_6\text{Mo}_7\text{O}_{24} \cdot 4\text{H}_2\text{O}$ were dissolved in formic acid. The obtained solutions were evaporated and dried at 473 K in air. The resulting powders were sintered gradually at 873 K for 6 h in air to remove organic components. To obtain single-phase materials, a two-stage annealing process was performed, at 1173 and 1473 K for 3 h in a H_2 - H_2O (3%) gas mixture. The elemental composition of the prepared samples was characterized by atomic-emission spectroscopy (AES) with plasma analysis, using a Perkin Elmer Optima 4300 DV spectrometer (PerkinElmer, Waltham, MA, USA). Powders were pressed at 400 MPa into

bulk ceramic samples and formed by annealing at 1473 K for 3 h in a H₂-H₂O(3%) gas mixture. The heating and cooling rate was 3 K min⁻¹.

The phase composition and structure of as-prepared powders and ceramics were studied at room temperature via X-ray diffraction (XRD) analysis, using a Rigaku DMAX diffractometer (Rigaku, Tokyo, Japan) with Cu_{Kα} radiation with step $2\theta = 0.02^\circ$. The phase analysis was based on the PDF-2 database. Unit cell parameters were calculated based on interplanar distances using CellRef v.3.0 software. The morphology of ceramic samples was investigated via scanning electron microscopy (SEM) in a Tescan MIRA 3 LMU microscope (Tescan, Brno, Czech Republic) using secondary electron (SE) and back-scattered electron (BSE) operating modes. The original surface of ceramic samples was examined without pretreatment or etching. The maps of elemental distributions were obtained via energy-dispersive X-ray spectroscopy (EDX), using an Oxford Instruments X-Max 80 INCA Energy 350 microanalysis system with a non-nitrogen detector (Oxford Instruments, Abingdon, UK). Measurements of the relative density of the ceramic samples were carried out according to the Archimedes method, by weighing them in kerosene on CAS CAUX 220 analytical scales (CAS, Seoul, South Korea). High-resolution transmission electron microscopy (HRTEM) analysis was used for the refinement of microstructure of powder samples. HRTEM analysis was performed using JEM-2010 equipment (JEOL, Tokyo, Japan), operating at a line resolution of 0.14 nm. Microanalysis of elemental composition by EDX analysis (XFlash, Bruker, Billerica, MA, USA) was used, with an Si detector at 127 eV resolution. For preparation of the samples for HRTEM observation, a drop of the specimen in suspension, ultrasonically treated in ethanol, was placed into a holey-carbon film supported on Cu grids.

The measurements of electrical conductivity, Seebeck coefficient and linear expansion were performed at 1073 K in a N₂-H₂-H₂O gas mixture with an a_{O_2} range of 10^{-21} to 10^{-15} atm. The composition of the N₂-H₂-H₂O gas mixture was set by an electrochemical pump based on an yttria-stabilized zirconia (YSZ) ceramic test tube. The oxygen activity (a_{O_2}) was controlled using an electrochemical sensor, also based on YSZ. Humidity was set by bubbling of gas mixture through water at room temperature. Electrical conductivity measurements were performed by 4-probe DC method using a Hioki RM-3542 microohmmeter (Hioki, Nagano, Japan). The samples were rectangular bars with four Pt electrodes, made of dispersed Pt powder and sintered at 1373 K for 1 h in a N₂-H₂-H₂O gas mixture. Seebeck coefficients were measured using a state-of-the-art setup based on L-card 24-bit ADC. Several open circuit voltage (OCV) values were collected at a series of temperature gradients ($\Delta T = 0-15$ K) by means of a built-in micro heater in the measuring cell. The Seebeck coefficient was calculated by the slope of the OCV = $f(\Delta T)$ dependency. The Seebeck coefficient of $-18.25 \mu V K^{-1}$ for Pt wires at 1073 K [41] was taken into account. The linear expansion of ceramics with atmospheric composition (chemical expansion) was investigated using dilatometry. A quartz dilatometer based on TESA Tesatronic TT-80 equipment with a GT-21HP probe (TESA, Renens, Switzerland) was used. The sample length at 1073 K and $a_{O_2} = 10^{-19.5}$ atm (corresponding to the value of OCV = 1 V on the oxygen electrochemical sensor) was taken as the reference point for the relative expansion.

3. Results and Discussion

3.1. Materials Characterization

Figure 1 shows XRD patterns of as-prepared CaV_{1-x}Mo_xO_{3-δ} ($0.3 \leq x \leq 0.5$) samples. A low content of metallic Mo was found in some samples. Also possible are minor impurities of CaO, monoclinic Ca₃V₂O₈ or Ca₂V₂O₇, which are beyond the XRD detection line. In general, the chemical composition of the prepared samples conformed to initial reagent concentration, according to AES analysis.

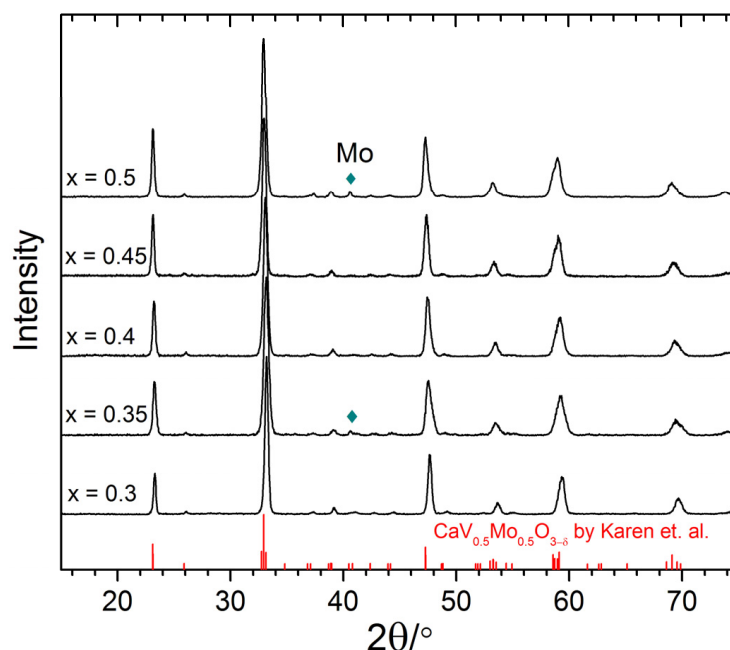


Figure 1. XRD patterns of as-prepared $\text{CaV}_{1-x}\text{Mo}_x\text{O}_{3-\delta}$ ($0.3 \leq x \leq 0.5$) powders.

The crystal structure of $\text{CaV}_{1-x}\text{Mo}_x\text{O}_{3-\delta}$ solid solutions is described within the orthorhombic perovskite lattice with the $Pnma$ space group, as reported for $\text{CaVO}_{3-\delta}$ [3] and $\text{CaMoO}_{3-\delta}$ [4], as well as for $\text{CaV}_{0.5}\text{Mo}_{0.5}\text{O}_{3-\delta}$ [7,42]. With an increase in the Mo concentration in $\text{CaV}_{1-x}\text{Mo}_x\text{O}_{3-\delta}$, the XRD peaks shift to smaller angles, indicating an increase in the unit cell parameters as the ionic radii of Mo are larger than V (for the average 4+ state). Figure 2 presents the calculated unit cell parameters of the orthorhombic cell of $\text{CaV}_{1-x}\text{Mo}_x\text{O}_{3-\delta}$. A bend on the dependence of the b and c unit cell parameters occurs, whereas the a parameter behaves linearly. A similar effect in the form of a structural transition from cubic to tetragonal syngony in $\text{SrFe}_{1-x}\text{Mo}_x\text{O}_{3-\delta}$ at the Mo concentration $x = 0.4$ was found in [43]. Subsequently, the authors of [44] found that, with an increase in the Mo concentration in $\text{SrFe}_{1-x}\text{Mo}_x\text{O}_{3-\delta}$, the fraction of ordered regions of the double perovskite $\text{Sr}_2\text{FeMoO}_6$ gradually increases. Merkulov et al. [45] confirmed the ordering of Fe and Mo at the level of nanosized domains as the double perovskite $\text{Sr}_2\text{FeMoO}_6$, within a disordered matrix of the orthorhombic perovskite of $\text{SrFe}_{0.7}\text{Mo}_{0.3}\text{O}_{3-\delta}$. However, Karen et al. [7] showed, via synchrotron X-ray powder diffraction analysis, the absence of ordering of V and Mo in the B site of $\text{CaV}_{0.5}\text{Mo}_{0.5}\text{O}_{3-\delta}$, thus the formation of a double perovskite structure Ca_2VMoO_6 is extremely unlikely. Therefore, XRD analysis does not provide an understanding of the structural differences in a number of $\text{CaV}_{1-x}\text{Mo}_x\text{O}_{3-\delta}$ ($0.3 \leq x \leq 0.5$) solid solutions.

Figure S1 in the Supplementary Materials shows SEM images (SE mode) of sintered $\text{CaV}_{1-x}\text{Mo}_x\text{O}_{3-\delta}$ ($0.3 \leq x \leq 0.5$) ceramic samples. A high porosity of about 35% can be observed, which is also confirmed by measurements via the Archimedes method. A high porosity of ceramics is characteristic of such compounds [7,17]. Most of the ceramic grains under study are approximately a few μm in size, with many grains forming large agglomerates measuring 5–10 μm in size. Samples $\text{CaV}_{0.7}\text{Mo}_{0.3}\text{O}_{3-\delta}$ and $\text{CaV}_{0.5}\text{Mo}_{0.5}\text{O}_{3-\delta}$ show a wide variation in grain sizes, while $\text{CaV}_{0.6}\text{Mo}_{0.4}\text{O}_{3-\delta}$ shows a more even distribution of grain sizes.

The results from a more detailed SEM study of ceramics, with the use of the BSE mode, are shown in Figure 3. Samples $\text{CaV}_{0.7}\text{Mo}_{0.3}\text{O}_{3-\delta}$ and $\text{CaV}_{0.5}\text{Mo}_{0.5}\text{O}_{3-\delta}$ shows a homogeneous image, with the exception of small light grains that are impurities of metallic Mo, as recorded on the XRD diagrams. On the contrary, sample $\text{CaV}_{0.6}\text{Mo}_{0.4}\text{O}_{3-\delta}$ demonstrates contrast, indicating a difference in the chemical composition of individual

grains. Unfortunately, the complex relief of the samples does make it possible to obtain an adequate EDX analysis of elemental concentrations.

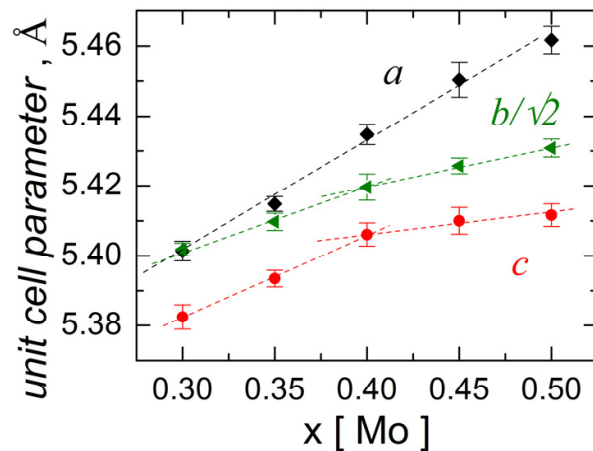


Figure 2. The dependence of a , b and c unit cell parameters ($Pnma$ space group) of $\text{CaV}_{1-x}\text{Mo}_x\text{O}_{3-\delta}$ on Mo concentration.

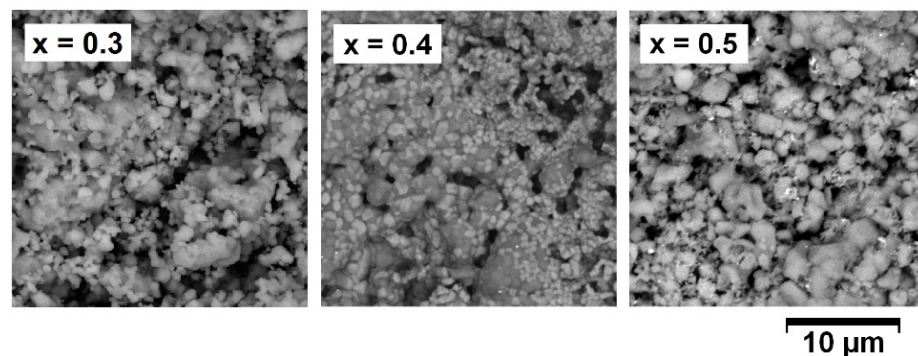


Figure 3. SEM images (BSE mode) of the surface of $\text{CaV}_{1-x}\text{Mo}_x\text{O}_{3-\delta}$ ($x = 0.3, 0.4, 0.5$) ceramic samples.

A detailed study of the $\text{CaV}_{0.6}\text{Mo}_{0.4}\text{O}_{3-\delta}$ and $\text{CaV}_{0.5}\text{Mo}_{0.5}\text{O}_{3-\delta}$ powders was performed via HRTEM. The $\text{CaV}_{0.5}\text{Mo}_{0.5}\text{O}_{3-\delta}$ powder sample is present as well crystallized particles of the perovskite phase, with a size of about 1 μm . The interplanar distance of 2.165 \AA observed in Figure 4a corresponds to the $\{022\}$ set for the orthorhombic perovskite lattice. For convenience, we have provided real resolution HRTEM images in the Supplementary Materials. The EDX data on the surface of the observed particles, in general, corresponds to the chemical composition established during the synthesis. However, it should be noted that regions with an increased content of Ca cations are recorded, which corresponds to the enrichment of the perovskite surface with calcium oxide. Previously, Ca segregation was detected via X-ray photoelectron spectroscopy [39]. The Cu reflex on the EDX spectrum is due to the Cu mesh that was used as a powder holder.

Figure 4b shows the HRTEM results for the $\text{CaV}_{0.6}\text{Mo}_{0.4}\text{O}_{3-\delta}$ powder sample, which demonstrates a large scattering in crystallite sizes, from 50 nm to 500 nm. According to EDX data, crystallites have different chemical compositions; firstly, the contents of V and Mo differ. Three characteristic regions can be found: enriched in Mo (region 1); with an equal ratio of V and Mo (region 2); or enriched in V (region 3). In all cases, the sets of interplanar spacings for $\text{CaV}_{0.6}\text{Mo}_{0.4}\text{O}_{3-\delta}$ are well-described within the orthorhombic perovskite lattice, which is also the case for the $\text{CaV}_{0.5}\text{Mo}_{0.5}\text{O}_{3-\delta}$ sample. Thus, the $\text{CaV}_{0.6}\text{Mo}_{0.4}\text{O}_{3-\delta}$ sample is characterized by phase separation into nanosized regions with different cationic compositions, which have a similar crystal structure. This fact explains the observed single-phase state of $\text{CaV}_{0.6}\text{Mo}_{0.4}\text{O}_{3-\delta}$, according to XRD (Figure 1), which does not show significant

peak broadening. The phase decomposition often occurs in solid solutions with limited component solubility [46], as well as separation of the main crystal lattice into two or more lattices. For example, such cases of phase separation are observed in disordered perovskite phases, in the form of partial ordering in nanoscale domains with a double perovskite structure [45,47]. However, almost nothing is known about phase separation into completely isostructural phases. It is possible that this phenomenon is caused by a peculiar distribution of the charge states of V and Mo, by analogy with the effect of Re in solid solutions of $V_{1-x}Re_xO_2$ with a rutile structure [48]. Previously, we observed an anomalous distribution of the charge states of $V^{3+/4+}$ in $CaV_{0.6}Mo_{0.4}O_{3-\delta}$, according to X-ray photoelectron spectroscopy analysis [39]. The most surprising fact is that the phase separation of the material occurs within a very limited region of $CaV_{1-x}Mo_xO_{3-\delta}$ solid solutions, near the Mo concentration $x = 0.4$. Further structural clarifications are necessary in order to understand how $CaV_{1-x}Mo_xO_{3-\delta}$ solid solutions differ above and below $x = 0.4$.

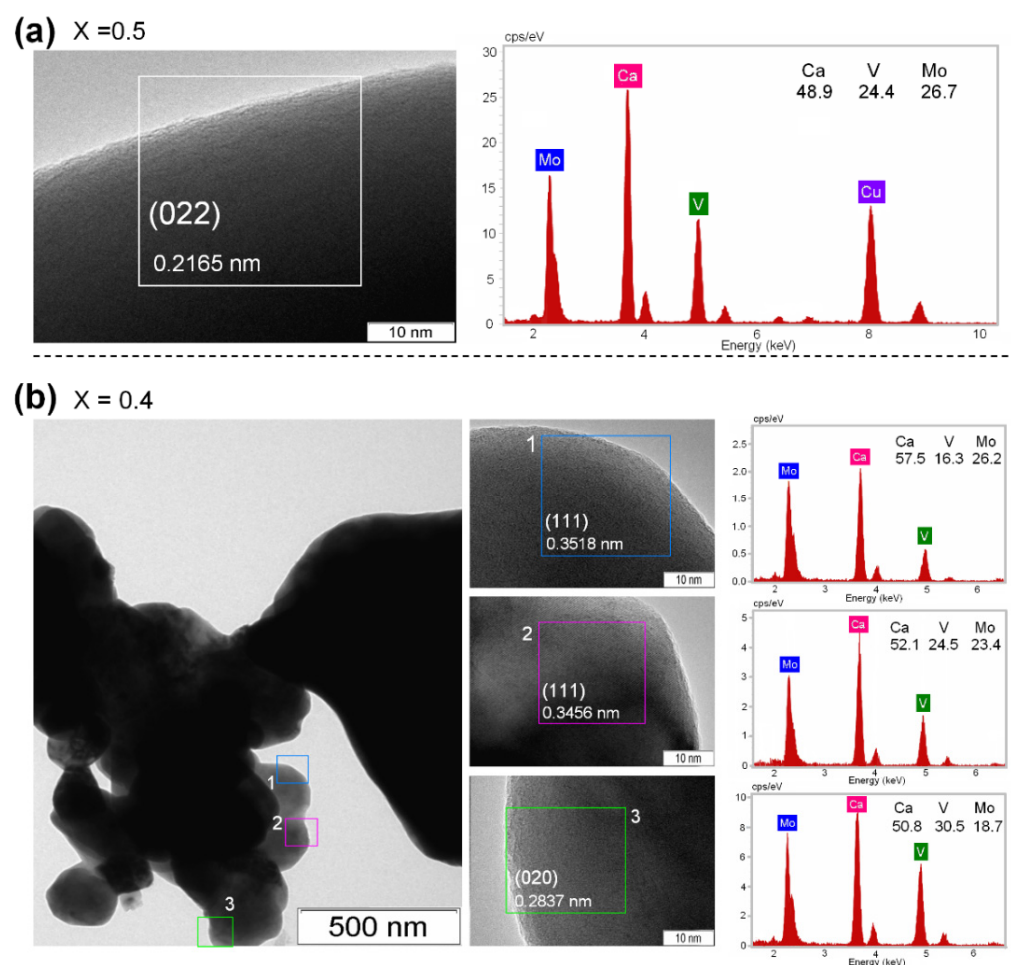


Figure 4. HRTEM images of $CaV_{0.5}Mo_{0.5}O_{3-\delta}$ (a) and $CaV_{0.6}Mo_{0.4}O_{3-\delta}$ (b) powders with results of EDX elemental analysis.

3.2. Impact of aO_2 on Properties of the Materials

The main course of measurements of electrical conductivity and chemical expansion was carried out under highly reducing conditions, at $aO_2 = 10^{-21}$ atm with a gradual increase in oxygen activity up to $aO_2 = 10^{-15}$ atm with reverse for checking thermodynamic equilibrium. We observed a long equilibration of approximately 20 h for each experimental point. Taking into account the temperature of 1073 K and the high porosity of the samples, it is difficult to connect the above fact with the diffusion of oxygen through the sample. Most likely, the long time taken in reaching equilibrium is due to the diffusion of cations.

For example, a change in the mutual ordering of V and Mo can be expected, as earlier studies [7] showed the absence of long-range order between V and Mo in the crystal lattice of $\text{CaV}_{0.5}\text{Mo}_{0.5}\text{O}_{3-\delta}$.

Figure 5a shows the conductivity dependencies on $a\text{O}_2$ of $\text{CaV}_{1-x}\text{Mo}_x\text{O}_{3-\delta}$ ($0.3 \leq x \leq 0.5$) ceramic samples at 1073 K. The dependences are nonmonotonic and have a maximum in the region of $a\text{O}_2 = 10^{-19}$ atm. At the same time, the Seebeck coefficient for $\text{CaV}_{1-x}\text{Mo}_x\text{O}_{3-\delta}$ at 1073 K is nearly independent of $a\text{O}_2$ (Figure 5b). As the main charge carriers in $\text{CaV}_{1-x}\text{Mo}_x\text{O}_{3-\delta}$ are delocalized electrons [7,38], the change in the conductivity of materials with varying $a\text{O}_2$ should primarily be associated with their concentration and mobility. The electron mobility depends on the type of electron scattering. Earlier, we showed the mixed character of electron scattering in $\text{CaV}_{1-x}\text{Mo}_x\text{O}_{3-\delta}$, which is intermediate between electron–phonon and electron–electron [38].

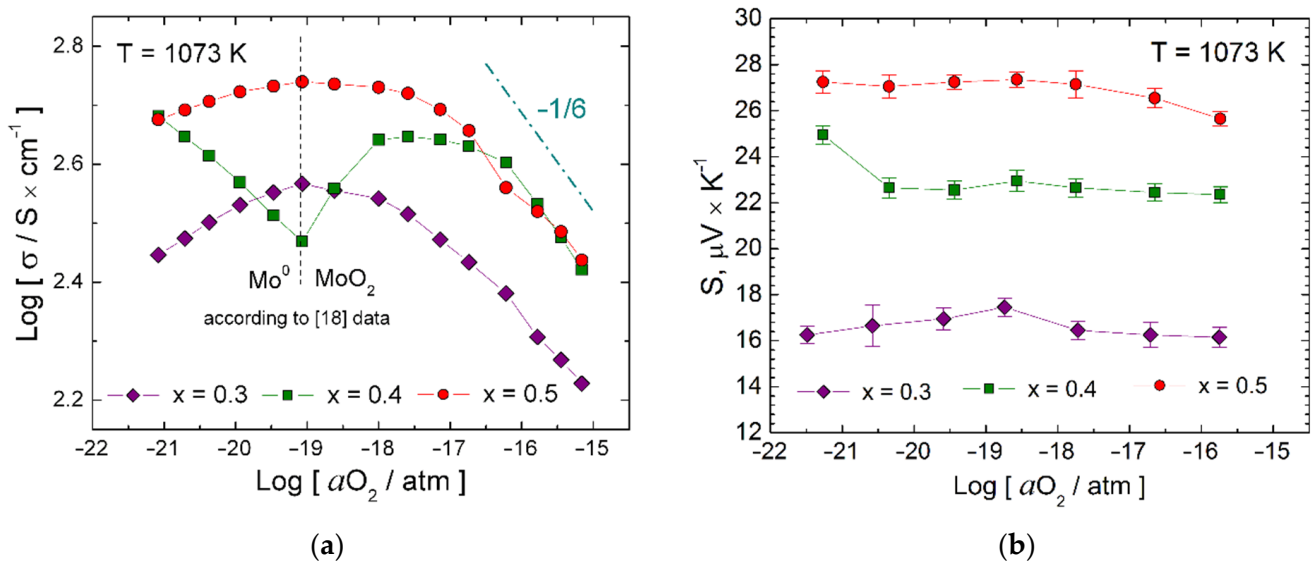


Figure 5. The dependencies of conductivity (a) and Seebeck coefficient (b) of $\text{CaV}_{1-x}\text{Mo}_x\text{O}_{3\pm\delta}$ ($0.3 \leq x \leq 0.5$) ceramics on $a\text{O}_2$ at 1073 K.

It is known that in conventional metallic conductors, the concentration of free electrons is nearly independent of external conditions. At the same time, for oxide materials in the region of small $a\text{O}_2$ values, Brower's model assumes the formation of oxygen vacancies ($\text{V}_\text{O}^{\bullet\bullet}$) from oxygen in crystal lattice sites (O_O^\times) with the generation of two n-type electrons (e^-) per vacancy, according to the equation



In this case, the slope of the logarithmic dependence of the concentration of electronic defects on $a\text{O}_2$ will correspond to $-1/6$, in the case of the electronic type of disordering [49]. In Figure 5a, it can be seen that the slope of the logarithmic dependences of conductivity in the $a\text{O}_2$ region from 10^{-15} – 10^{-19} atm is less than the expected value ($-1/6$), which might be associated with a decrease in the electron mobility. The authors of [29] came to a similar conclusion when studying the effect of oxygen nonstoichiometry on the conductivity of $\text{CaVO}_{3-\delta}$, assuming additional scattering of electrons by oxygen vacancies. Likewise, a similar suggestion was given in [50] while studying the conductivity of $\text{SrV}_{1-x}\text{Nb}_x\text{O}_{3-\delta}$ systems. The effect of oxygen vacancies on the electronic structure of SrVO_3 was recently discussed in [37], where it was demonstrated that the shape of the Mott–Hubbard band changes under the influence of created oxygen vacancies.

The presence of a clear maximum of conductivity at $a\text{O}_2 = 10^{-19}$ atm (Figure 5a), with a subsequent decrease in conductivity at lower $a\text{O}_2$, is difficult to correlate with the influence of one type of electron scattering. Similar dependencies of conductivity with

a maximum were observed by Macias et al. for $\text{SrVO}_{3-\delta}$ [16] and substituted strontium vanadates [15,17,50], where the behavior of conductivity under highly reducing conditions was explained by the transition of vanadium from V^{3+} to V^{4+} . In addition, the observed phenomenon is similar to the data reported by Hui and Petric [18] for the MoO_2 – Mo transition at 1073 K (dashed line in Figure 5a). In the region of $a\text{O}_2$ less than 10^{-19} atm, the behavior of $\text{CaV}_{1-x}\text{Mo}_x\text{O}_{3-\delta}$ can be described by the equilibrium of the main perovskite phase with the phase of metallic Mo. This is confirmed by the XRD pattern of $\text{CaV}_{0.5}\text{Mo}_{0.5}\text{O}_{3-\delta}$ (Figure 6) obtained after holding for 54 h at $a\text{O}_2 = 10^{-21}$ atm, which shows an admixture of metallic Mo. At the same time, after holding at $a\text{O}_2 = 10^{-19}$ atm, we can observe the disappearance of the Mo impurity and the appearance of XRD reflections of the tetragonal phase of CaMoO_4 . After holding at $a\text{O}_2 = 10^{-17}$ atm, the concentration of the CaMoO_4 tetragonal phase increases. The high metal-like conductivity of the material remains up to $a\text{O}_2 = 10^{-15}$ atm. A long process of the degradation of electrical conductivity of $\text{CaV}_{0.5}\text{Mo}_{0.5}\text{O}_{3\pm\delta}$ begins at $a\text{O}_2 > 10^{-15}$ atm. Figure 6 shows XRD patterns of the surface of the ceramic sample after 54 h of exposure at $a\text{O}_2 = 10^{-14.7}$ atm, where the complete decomposition of the perovskite-like phase into CaMoO_4 with a tetragonal structure and $\text{Ca}_3\text{V}_2\text{O}_8$ with a monoclinic structure can be observed. Thus, the decrease in the conductivity of $\text{CaV}_{0.5}\text{Mo}_{0.5}\text{O}_{3\pm\delta}$ in the region near $a\text{O}_2 > 10^{-19}$ atm occurs due to the progressive decomposition of the metal-like phase into two insulating phases, which is clearly seen from the evolution of XRD patterns in Figure 6. For comparison, an XRD pattern of the $\text{CaV}_{0.5}\text{Mo}_{0.5}\text{O}_{3-\delta}$ powder after oxidation in air at 1473 K is shown, in which only the calcium molybdate phase with a tetragonal structure remains; whereas, $\text{Ca}_3\text{V}_2\text{O}_8$ with a monoclinic structure can transform into $\text{Ca}_2\text{V}_2\text{O}_7$ with a pyrochlore structure, which, at temperatures above 1273 K, transforms into an amorphous form [42]. Figure 7 shows SEM images of the surfaces of oxidized samples. One can see the higher density of the oxidized ceramics relative to the originals, which indicates sintering during the decomposition of the perovskite phase. Unfortunately, the resolution of the EDX detector does not allow us to estimate the distribution of elements, although some uneven distribution of V and Mo is observed for sample $\text{CaV}_{0.5}\text{Mo}_{0.5}\text{O}_{3\pm\delta}$. The $a\text{O}_2$ –boundary for $\text{CaV}_{0.5}\text{Mo}_{0.5}\text{O}_{3\pm\delta}$, where high metal-like conductivity is found, can be considered as the $a\text{O}_2$ region near approximately 10^{-16} atm, which is in agreement with [42], and is also in good agreement with [16] for $\text{SrVO}_{3-\delta}$.

Figure 8 demonstrates chemical expansion and electrical conductivity dependencies on $a\text{O}_2$ for $\text{CaV}_{1-x}\text{Mo}_x\text{O}_{3-\delta}$ ($x = 0.4$ and 0.5) at 1073 K. An increase in $a\text{O}_2$ from 10^{-21} up to 10^{-19} atm causes a linear compression of the $\text{CaV}_{0.5}\text{Mo}_{0.5}\text{O}_{3-\delta}$ ceramic sample, due to a decrease in the ionic radii of V and Mo with an increase in their oxidation state, which is consistent with conventional concepts [51,52]. In the region of $a\text{O}_2 = 10^{-17.5}$ atm, a minimum of chemical expansion can be observed, after which the sample begins to expand up to $a\text{O}_2 = 10^{-16}$ atm, and finally an intensive expansion of the sample occurs. This is due to the partial decomposition of $\text{CaV}_{0.5}\text{Mo}_{0.5}\text{O}_{3-\delta}$ according to the XRD results (Figure 6). Figure 8b shows the dependencies of conductivity and linear expansion of $\text{CaV}_{0.6}\text{Mo}_{0.4}\text{O}_{3-\delta}$ on $a\text{O}_2$ at 1073 K, which differ significantly from the behavior of the $\text{CaV}_{0.5}\text{Mo}_{0.5}\text{O}_{3-\delta}$ sample. The conductivity of $\text{CaV}_{0.6}\text{Mo}_{0.4}\text{O}_{3-\delta}$ shows nonmonotonic changes at $a\text{O}_2 < 10^{-18}$ atm and has a local minimum at $a\text{O}_2 = 10^{-19}$ atm. The chemical expansion of the $\text{CaV}_{0.6}\text{Mo}_{0.4}\text{O}_{3-\delta}$ ceramic sample demonstrates a difficult-to-explain relationship that does not agree with conventional concepts. Taking into account the phase separation in the $\text{CaV}_{0.6}\text{Mo}_{0.4}\text{O}_{3-\delta}$ sample into nanoscale regions with different chemical compositions, as detected via HRTEM, it can be assumed that the defect structure of the material will show a composite nature.

Figure 9a demonstrates the long-term relaxation of the chemical expansion of $\text{CaV}_{1-x}\text{Mo}_x\text{O}_{3-\delta}$ over several tens of hours. Upon a change in $a\text{O}_2$ from $10^{-16.7}$ to $10^{-16.2}$ atm for the $\text{CaV}_{0.5}\text{Mo}_{0.5}\text{O}_{3\pm\delta}$ sample and from $10^{-15.8}$ to $10^{-15.3}$ atm for the $\text{CaV}_{0.6}\text{Mo}_{0.4}\text{O}_{3\pm\delta}$ sample there is a long process of expansion, during which there is a significant change in its linear dimensions. The absorption of oxygen is accompanied by the formation of monoclinic

$\text{Ca}_3\text{V}_2\text{O}_8$ and tetragonal CaMoO_4 phases from perovskite-like $\text{CaV}_{1-x}\text{Mo}_x\text{O}_{3-\delta}$, which leads to intense chemical expansion. A small difference in the a_{O_2} values is associated with different concentrations of the V–Mo pair. The mechanism of kinetics of chemical expansion relaxation was investigated using a dependency approach of degree of transformation ($(\Delta L/L)_{\text{normalized}}$) on reduced time ($t/t_{0.5}$) [53]. Several basic mechanisms of solid-state reactions were considered: diffusion of components controlled reaction, solid-state reaction following first order kinetics, phase boundary controlled reaction, and Avrami–Erofeev kinetic equation under limitations, due to the nucleation stage of the reaction. The form of typical dependences of $(\Delta L/L)_{\text{normalized}} = f(t/t_{0.5})$ for various mechanisms of solid-phase reactions with experimental data is shown in Figure 9b. It can be concluded that the closest correspondence to the relaxation dependence of the chemical expansion of $\text{CaV}_{1-x}\text{Mo}_x\text{O}_{3\pm\delta}$ samples is related to the solid-phase reaction mechanism, in good agreement with the observed decomposition of the perovskite-like $\text{CaV}_{0.5}\text{Mo}_{0.5}\text{O}_{3-\delta}$ into tetragonal CaMoO_4 and monoclinic $\text{Ca}_3\text{V}_2\text{O}_8$.

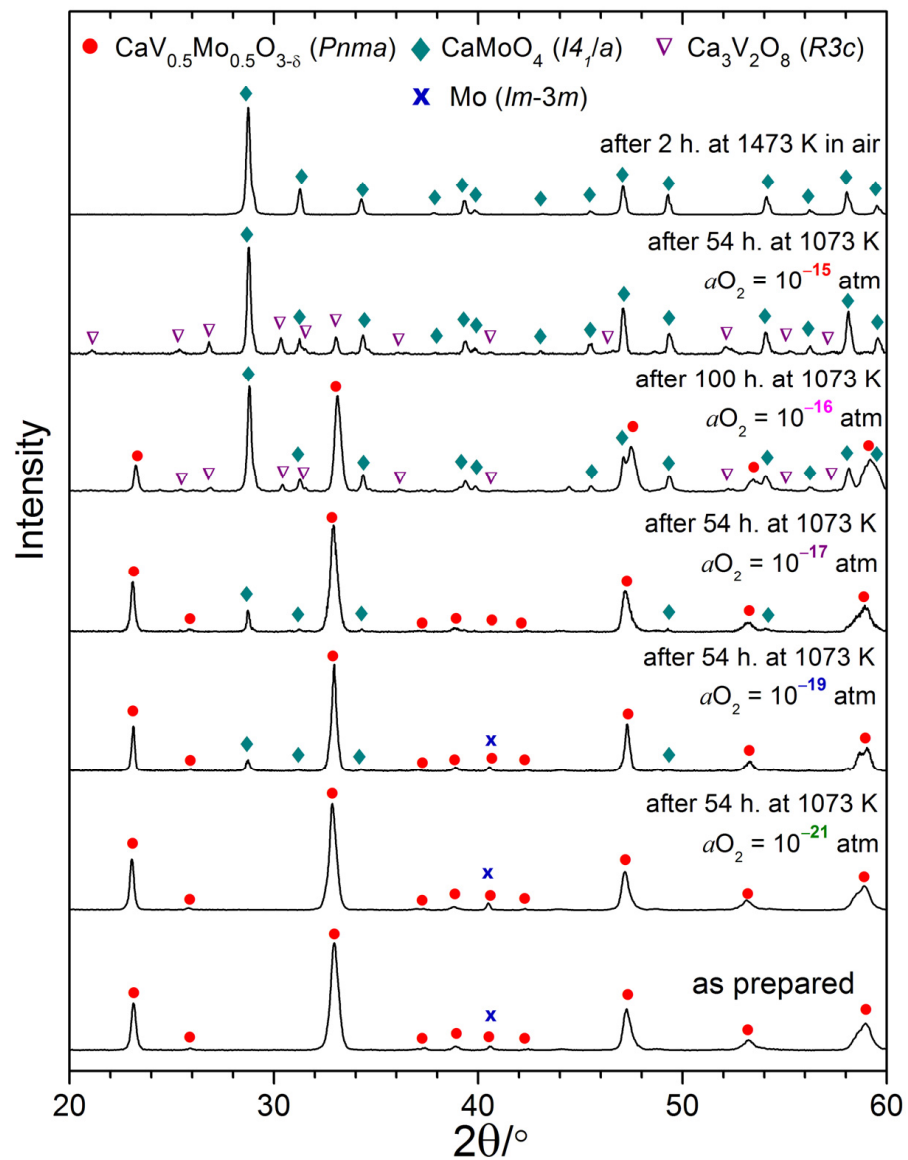


Figure 6. XRD patterns of $\text{CaV}_{0.5}\text{Mo}_{0.5}\text{O}_{3\pm\delta}$ samples after an exhibition at various conditions.

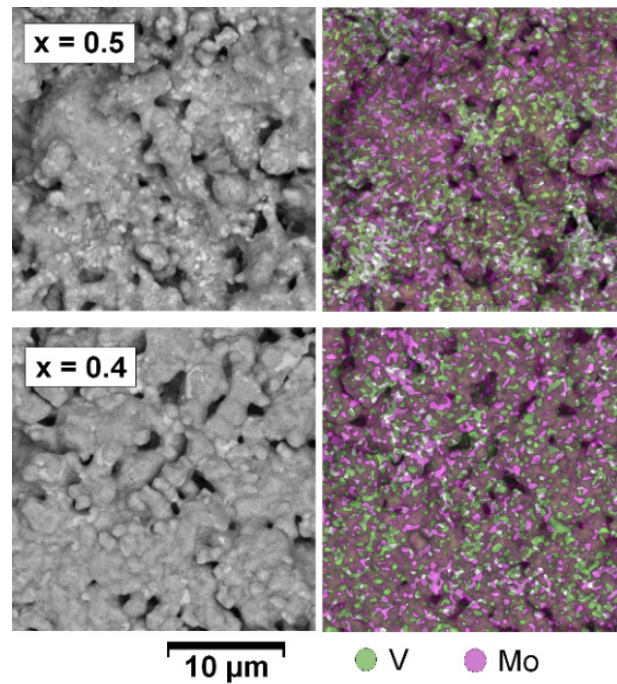


Figure 7. SEM images (BSE mode) of surface of $\text{CaV}_{1-x}\text{Mo}_x\text{O}_{3\pm\delta}$ ($x = 0.4$ and 0.5) ceramic samples after oxidation at 1073 K and $a_{\text{O}_2} = 10^{-15}$ atm with EDX maps of V and Mo distribution.

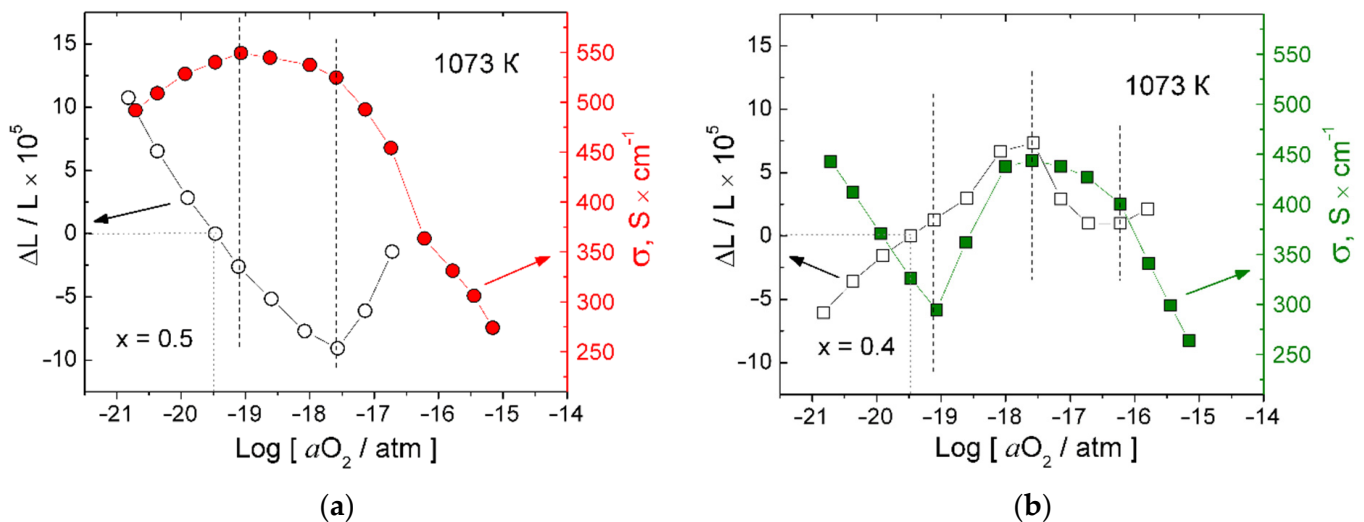


Figure 8. The dependencies of chemical expansion (left axes) and conductivity (right axes) on a_{O_2} at 1073 K for: $\text{CaV}_{0.5}\text{Mo}_{0.5}\text{O}_{3\pm\delta}$ (a) and $\text{CaV}_{0.6}\text{Mo}_{0.4}\text{O}_{3\pm\delta}$ (b).

The behavior of the electrical properties of the individual $\text{CaV}_{1-x}\text{Mo}_x\text{O}_{3\pm\delta}$ perovskite phases from a_{O_2} remains poorly understood against the background of the phase decomposition. The positive sign of the Seebeck coefficient (Figure 5b) indicates that the delocalized electrons in $\text{CaV}_{1-x}\text{Mo}_x\text{O}_{3\pm\delta}$ are p-type electrons (electronic holes) in the entire studied area of a_{O_2} . In addition, small changes in the conductivity and Seebeck coefficient indicate a small effect of a_{O_2} on the concentration and mobility of delocalized p-type electrons in $\text{CaV}_{1-x}\text{Mo}_x\text{O}_{3\pm\delta}$, although the opposite was expected. Apparently, $\text{CaV}_{1-x}\text{Mo}_x\text{O}_{3\pm\delta}$ has a very small region of oxygen nonstoichiometry, which causes its progressive decomposition with an increase or decrease in a_{O_2} . Accordingly, significant changes in the crystal and electronic structure of the $\text{CaV}_{1-x}\text{Mo}_x\text{O}_{3\pm\delta}$ perovskite phase itself are not expected.

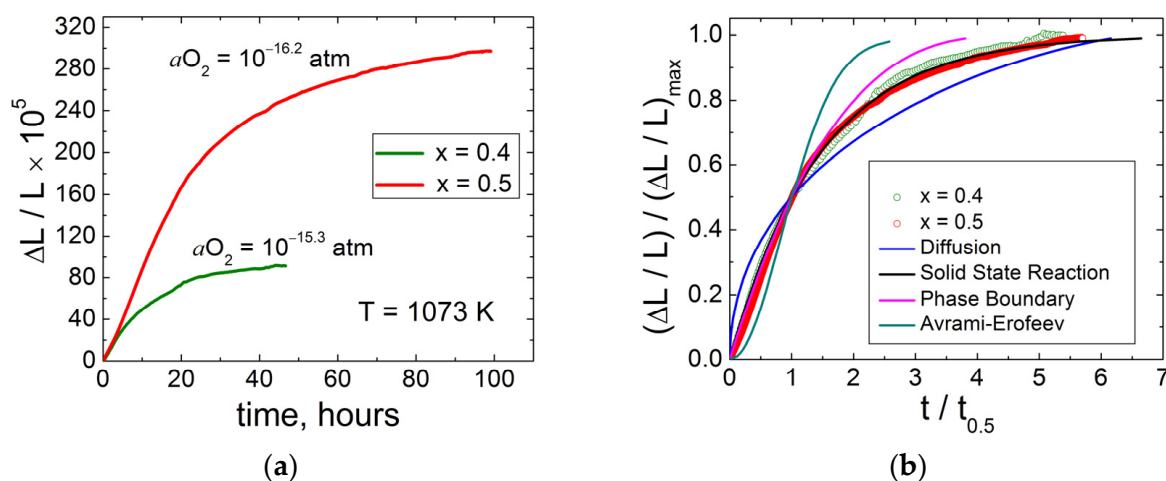


Figure 9. The results of chemical expansion study of oxidation process in $\text{CaV}_{1-x}\text{Mo}_x\text{O}_{3\pm\delta}$ ($x = 0.4$ and 0.5) at 1073 K and constant a_{O_2} value in $\Delta L/L = f(t)$ (a) and $(\Delta L/L)_{\text{normalized}} = f(t/t_{0.5})$ (b) plots.

4. Conclusions

Solid solutions $\text{CaV}_{1-x}\text{Mo}_x\text{O}_{3-\delta}$ with an orthorhombic perovskite structure near the structural transition at $x = 0.4$ were considered, and showed a bend in the dependencies of b and c unit cell parameters on the Mo concentration. The phase separation of $\text{CaV}_{0.6}\text{Mo}_{0.4}\text{O}_{3-\delta}$ into nanoscale regions with different contents of V and Mo was observed. It is noteworthy that phase separation occurs within a narrow range of V and Mo concentrations. We see no reason to classify the regions of $\text{CaV}_{1-x}\text{Mo}_x\text{O}_{3-\delta}$ solid solutions before and after $x = 0.4$ as fundamentally different types of solid solutions, although further structural refinements are needed.

The article considers the behaviors of conductivity and chemical expansion of $\text{CaV}_{1-x}\text{Mo}_x\text{O}_{3\pm\delta}$ at 1073 K depending on the activity of oxygen in the gas phase (a_{O_2}), under the reducing conditions of a $\text{N}_2\text{-H}_2\text{-H}_2\text{O}$ gas mixture. Both types of dependencies exhibit nonmonotonic behavior. Despite the expected significant effect of a_{O_2} on the concentration and mobility of delocalized p-type electrons in $\text{CaV}_{1-x}\text{Mo}_x\text{O}_{3\pm\delta}$, the phase decomposition causes major changes in electrical conductivity and chemical expansion of the materials under study. In the reduction region at a_{O_2} less than 10^{-19} atm, there is a phase equilibrium with metallic Mo, while the oxidation of materials at $a_{\text{O}_2} > 10^{-19}$ atm is accompanied by the progressive decomposition of the metal-like perovskite V–Mo phase into insulating tetragonal calcium molybdate and monoclinic calcium vanadate, and at $a_{\text{O}_2} = 10^{-15}$ atm, complete decomposition is observed.

Supplementary Materials: The following supporting information can be downloaded at: <https://www.mdpi.com/article/10.3390/cryst12030419/s1>. Figure S1: SEM images (SE mode) of the surface of sintered $\text{CaV}_{1-x}\text{Mo}_x\text{O}_{3-\delta}$ ($0.3 \leq x \leq 0.5$) ceramic samples; Figure S2: Real-resolution HRTEM image supported by FFT diffraction patterns for $\text{CaV}_{0.5}\text{Mo}_{0.5}\text{O}_{3-\delta}$ sample; Figure S3: Real-resolution HRTEM image supported by FFT diffraction patterns for $\text{CaV}_{0.6}\text{Mo}_{0.4}\text{O}_{3-\delta}$ sample (region 1); Figure S4: Real-resolution HRTEM image supported by FFT diffraction patterns for $\text{CaV}_{0.6}\text{Mo}_{0.4}\text{O}_{3-\delta}$ sample (region 2); Figure S5: Real-resolution HRTEM image supported by FFT diffraction patterns for $\text{CaV}_{0.6}\text{Mo}_{0.4}\text{O}_{3-\delta}$ sample (region 3).

Author Contributions: Conceptualization, S.A.B.; methodology, S.A.B. and A.V.K.; validation, S.A.B., E.Y.G. and A.V.K.; formal analysis, S.A.B. and E.Y.G.; investigation, S.A.B. and E.Y.G.; data curation, S.A.B. and A.V.K.; writing—original draft preparation, S.A.B.; writing—review and editing, A.V.K.; visualization, S.A.B.; supervision, S.A.B. All authors have read and agreed to the published version of the manuscript.

Funding: This research received no external funding.

Institutional Review Board Statement: Not applicable.

Informed Consent Statement: Not applicable.

Data Availability Statement: Not applicable.

Acknowledgments: The work was carried out using the equipment of the Center of Collective Use “Composition of matter” of Institute of High-Temperature Electrochemistry, UB RAS. HRTEM studies were conducted using the equipment of the Center of Collective Use “National Center of Catalyst Research” of the Borskov Institute of Catalysis, SB RAS. The authors are grateful to Plaksin S.V., Antonov B.D., Khodimchuk A.V. Moskalenko N.I. (all from IHTE UB RAS), and Farlenkov A.S. (Ural Federal University) for their assistance in the experiment.

Conflicts of Interest: The authors declare no conflict of interest. The funders had no role in the design of the study; in the collection, analyses, or interpretation of data; in the writing of the manuscript, or in the decision to publish the results.

References

1. Hayashi, S.; Aoki, R.; Nakamura, T. Metallic conductivity in perovskite-type compounds AMoO_3 ($A = \text{Ba, Sr, Ca}$) down to 2.5 K. *Mater. Res. Bull.* **1979**, *14*, 409–413. [\[CrossRef\]](#)
2. Inoue, I.H.; Goto, O.; Makino, H.; Hussey, N.E.; Ishikawa, M. Bandwidth control in a perovskite-type $3d^1$ -correlated metal $\text{Ca}_{1-x}\text{Sr}_x\text{VO}_3$. I. Evolution of the electronic properties and effective mass. *Phys. Rev. B* **1998**, *58*, 4372–4383. [\[CrossRef\]](#)
3. Falcón, H.; Alonso, J.A.; Casais, M.T.; Martínez-Lope, M.J.; Sánchez-Benítez, J. Neutron diffraction study and magnetotransport properties of stoichiometric CaVO_3 perovskite with positive magnetoresistance. *J. Solid State Chem.* **2004**, *177*, 3099–3104. [\[CrossRef\]](#)
4. de la Calle, C.; Alonso, J.A.; García-Hernández, M.; Pomjakushin, V. Neutron diffraction study and magnetotransport properties of stoichiometric CaMoO_3 perovskite prepared by a soft-chemistry route. *J. Solid State Chem.* **2006**, *179*, 1636–1641. [\[CrossRef\]](#)
5. Makino, H.; Inoue, I.H.; Rozenberg, M.J.; Aiura, Y.; Hase, I.; Onari, S. Band-width control in a perovskite-type $3d^1$ correlated metal $\text{Ca}_{1-x}\text{Sr}_x\text{VO}_3$. II. Optical spectroscopy investigation. *Phys. Rev. B* **1998**, *58*, 4384–4393. [\[CrossRef\]](#)
6. Mossaneck, R.J.O.; Abbate, M.; Yoshida, T.; Fujimori, A.; Yoshida, Y.; Shirakawa, N.; Eisaki, H.; Kohno, S.; Vicentin, F.C. Evolution of the spectral weight in the Mott-Hubbard series SrVO_3 - CaVO_3 - LaVO_3 - YVO_3 . *Phys. Rev. B* **2008**, *78*, 54–61. [\[CrossRef\]](#)
7. Karen, P.; Moodenbaugh, A.R.; Goldberger, J.; Santhosh, P.N.; Woodward, P.M. Electronic, magnetic and structural properties of A_2VMoO_6 perovskites ($A = \text{Ca, Sr}$). *J. Solid State Chem.* **2006**, *179*, 2120–2125. [\[CrossRef\]](#)
8. Nekrasov, I.A.; Keller, G.; Kondakov, D.E.; Kozhevnikov, A.V.; Pruschke, T.; Held, K.; Vollhardt, D.; Anisimov, V.I. Comparative study of correlation effects in CaVO_3 and SrVO_3 . *Phys. Rev. B* **2005**, *72*, 155106. [\[CrossRef\]](#)
9. Brahlek, M.; Zhang, L.; Lapano, J.; Zhang, H.-T.; Engel-Herbert, R.; Shukla, N.; Datta, S.; Paik, H.; Schlom, D.G. Opportunities in vanadium-based strongly correlated electron systems. *MRS Commun.* **2017**, *7*, 27–52. [\[CrossRef\]](#)
10. Zhang, L.; Zhou, Y.; Guo, L.; Zhao, W.; Barnes, A.; Zhang, H.-T.; Eaton, C.; Zheng, Y.; Brahlek, M.; Haneef, H.F.; et al. Correlated metals as transparent conductors. *Nat. Mater.* **2016**, *15*, 204–210. [\[CrossRef\]](#)
11. Gu, M.; Laverock, J.; Chen, B.; Smith, K.E.; Wolf, S.A.; Lu, J. Metal-insulator transition induced in CaVO_3 thin films. *J. Appl. Phys.* **2013**, *113*, 133704. [\[CrossRef\]](#)
12. Beck, S.; Schlauzero, G.; Chopra, U.; Ederer, C. Metal-insulator transition in CaVO_3 thin films: Interplay between epitaxial strain, dimensional confinement, and surface affects. *Phys. Rev. B* **2018**, *97*, 075107. [\[CrossRef\]](#)
13. McNally, D.E.; Lu, X.; Pellicciari, J.; Beck, S.; Dantz, M.; Naamneh, M.; Shang, T.; Medarde, M.; Schneider, C.W.; Strocov, V.N.; et al. Electronic localization in CaVO_3 films via bandwidth control. *Npj Quant. Mater.* **2019**, *4*, 6. [\[CrossRef\]](#)
14. Stoner, J.L.; Murgatroyd, P.A.E.; O’Sullivan, M.; Dyer, M.S.; Manning, T.D.; Claridge, J.B.; Rosseinsky, M.J.; Alaria, J. Chemical control of correlated metals as transparent conductors. *Adv. Funct. Mater.* **2019**, *29*, 1808609. [\[CrossRef\]](#)
15. Yaremchenko, A.A.; Brinkmann, B.; Janssen, R.; Frade, J.R. Electrical conductivity, thermal expansion and stability of Y- and Al-substituted SrVO_3 as prospective SOFC anode material. *Solid State Ion.* **2013**, *247–248*, 86–93. [\[CrossRef\]](#)
16. Macías, J.; Yaremchenko, A.A.; Frade, J.R. Redox transitions in strontium vanadates: Electrical conductivity and dimensional changes. *J. Alloys Compd.* **2014**, *601*, 186–194. [\[CrossRef\]](#)
17. Macías, J.; Yaremchenko, A.A.; Frade, J.R. Enhanced stability of perovskite-like SrVO_3 -based anode materials by donor-type substitution. *J. Mater. Chem.* **2016**, *A4*, 10186–10194. [\[CrossRef\]](#)
18. Hui, S.Q.; Petric, A. Conductivity and stability of SrVO_3 and mixed perovskites at low oxygen partial pressures. *Solid State Ion.* **2001**, *143*, 275–283. [\[CrossRef\]](#)
19. Macías, J.; Yaremchenko, A.A.; Rodríguez-Castellón, E.; Sarykevich, M.; Frade, J.R. Compromising between phase stability and electrical performance: SrVO_3 - SrTiO_3 solid solutions as solid oxide fuel cell anode components. *ChemSusChem* **2019**, *12*, 240–251. [\[CrossRef\]](#)
20. Brixner, L.H. X-ray study and electrical properties of system $\text{Ba}_x\text{Sr}_{(1-x)}\text{MoO}_3$. *J. Inorg. Nucl. Chem.* **1960**, *14*, 225–230. [\[CrossRef\]](#)

21. Ha, Y.; Lee, S. Oxygen-vacancy-endurable conductors with enhanced transparency using correlated $4d^2$ SrMoO_3 thin films. *Adv. Funct. Mater.* **2020**, *30*, 2001489. [[CrossRef](#)]
22. Kamata, K.; Nakamura, T.; Sata, T. Valence stability of molybdenum in alkaline earth molybdates. *Mater. Res. Bull.* **1975**, *10*, 373–378. [[CrossRef](#)]
23. Im, H.-N.; Jeon, S.-Y.; Choi, M.-B.; Kim, H.-S.; Song, S.-J. Chemical stability and electrochemical properties of $\text{CaMoO}_{3-\delta}$ for SOFC anode. *Ceram. Int.* **2012**, *38*, 153–158. [[CrossRef](#)]
24. Graves, C.R.; Reddy Sudireddy, B.; Mogensen, M.B. Molybdate based ceramic negative-electrode materials for solid oxide cells. *ECS Trans.* **2010**, *28*, 173–192. [[CrossRef](#)]
25. Osinkin, D.A. Kinetics of CO oxidation and redox cycling of $\text{Sr}_2\text{Fe}_{1.5}\text{Mo}_{0.5}\text{O}_{6-\delta}$ electrode for symmetrical solid state electrochemical devices. *J. Power Sources* **2019**, *418*, 17–23. [[CrossRef](#)]
26. Ueda, Y. Oxygen nonstoichiometry, structures, and physical properties of $\text{CaVO}_{3-\delta}$: I. A series of new oxygen-deficient phases. *J. Solid State Chem.* **1998**, *135*, 36–42. [[CrossRef](#)]
27. Ueda, Y.; Nakayama, N. Electron diffraction study of oxygen-defect perovskite $\text{CaVO}_{3-\delta}$. *Solid State Ion.* **1998**, *108*, 303–306. [[CrossRef](#)]
28. Iga, F.; Nishihara, Y. Metal-insulator transition with oxygen content in CaVO_{3-y} . *J. Phys. Soc. Jpn.* **1992**, *61*, 1867–1870. [[CrossRef](#)]
29. Inoue, I.H.; Morikawa, K.; Fukuchi, H.; Tsujii, T.; Iga, F.; Nishihara, Y. Metal-to-insulator transitions in CaVO_{3-y} . *Phys. B Condens. Matter* **1994**, *194–196*, 1067–1068. [[CrossRef](#)]
30. García-Jaca, J.; Mesa, J.L.; Insausti, M.; Larramendi, J.I.R.; Arriortua, M.I.; Rojo, T. Synthesis, crystal structure, stoichiometry and magnetic properties of $(\text{Ca}_{1-x}\text{Sr}_x)\text{VO}_3$. *Mater. Res. Bull.* **1999**, *34*, 289–301. [[CrossRef](#)]
31. Shikano, M.; Sakaebe, H.; Wakabayashi, N.; Higuchi, S. Structure and electrical properties of $\text{Sr}_{0.5}\text{Ca}_{0.5}\text{VO}_y$. *Solid State Ion.* **1998**, *108*, 327–332. [[CrossRef](#)]
32. Takeda, Y.; Kanno, K.; Takada, T.; Yamamoto, O.; Takano, M.; Nakayama, N.; Bando, Y. Phase relation in the oxygen nonstoichiometric system, SrFeO_x ($2.5 \leq x \leq 3.0$). *J. Solid State Chem.* **1986**, *63*, 237–249. [[CrossRef](#)]
33. Nakayama, N.; Takano, M.; Inamura, S.; Nakanishi, N.; Kosuge, K. Electron microscopy study of the “cubic” perovskite phase $\text{SrFe}_{1-x}\text{V}_x\text{O}_{2.5+x}$ ($0.05 \leq x \leq 0.1$). *J. Solid State Chem.* **1987**, *71*, 403–417. [[CrossRef](#)]
34. Savinskaya, O.; Nemudry, A.P. Oxygen transport properties of nanostructured $\text{SrFe}_{1-x}\text{Mo}_x\text{O}_{2.5+3/2x}$ ($0 < x < 0.1$) perovskites. *J. Solid State Electrochem.* **2011**, *15*, 269–275. [[CrossRef](#)]
35. Ancharova, U.V.; Cherepanova, S.V. Nano-domain states of strontium ferrites $\text{SrFe}_{1-y}\text{M}_y\text{O}_{2.5+x}$ ($M = \text{V}, \text{Mo}$; $y \leq 0.1$, $x \leq 0.2$). *J. Solid State Chem.* **2015**, *225*, 410–416. [[CrossRef](#)]
36. Inoue, I.H.; Bergemann, C.; Hase, I.; Julian, S.R. Fermi surface of $3d^1$ perovskite CaVO_3 near the Mott transition. *Phys. Rev. Lett.* **2002**, *88*, 236403. [[CrossRef](#)]
37. Backes, S.; Rödel, T.C.; Fortuna, F.; Frantzeskakis, E.; Le Fèvre, P.; Bertran, F.; Kobayashi, M.; Yukawa, R.; Mitsuhashi, T.; Kitamura, M.; et al. Hubbard band versus oxygen vacancy states in the correlated electron metal SrVO_3 . *Phys. Rev. B* **2016**, *94*, 241110. [[CrossRef](#)]
38. Belyakov, S.A.; Shkerin, S.N.; Kellerman, D.G.; Plekhanov, M.S. The effect of Mo concentration on the electrical properties of $\text{CaV}_{1-x}\text{Mo}_x\text{O}_{3-\delta}$ ($x = 0.2 \div 0.6$) anode material for solid oxide fuel cells. *Mater. Res. Bull.* **2020**, *129*, 110904. [[CrossRef](#)]
39. Belyakov, S.A.; Kuznetsov, M.V.; Shkerin, S.N. X-ray photoelectron spectroscopy study of $\text{CaV}_{1-x}\text{Mo}_x\text{O}_{3-\delta}$. *J. Solid State Chem.* **2018**, *262*, 301–308. [[CrossRef](#)]
40. Belyakov, S.A.; Shkerin, S.N.; Selezneva, N.V. Synthesis of an anode material based on mixed calcium vanadatomoxybdate and its stability in contact with solid electrolytes. *Russ. J. Appl. Chem.* **2015**, *88*, 706–710. [[CrossRef](#)]
41. Burkov, A.T.; Heinrich, A.; Konstantinov, P.P.; Nakama, T.; Yagasaki, K. Experimental set-up for thermopower and resistivity measurements at 100–1300 K. *Meas. Sci. Technol.* **2001**, *12*, 264–272. [[CrossRef](#)]
42. Aguadero, A.; de la Calle, C.; Alonso, J.A.; Pérez-Coll, D.; Escudero, M.J.; Daza, L. Structure, thermal stability and electrical properties of $\text{Ca}(\text{V}_{0.5}\text{Mo}_{0.5})\text{O}_3$ as solid oxide fuel cell anode. *J. Power Sources* **2009**, *192*, 78–83. [[CrossRef](#)]
43. Liu, G.Y.; Rao, G.H.; Feng, X.M.; Yang, H.F.; Ouyang, Z.W.; Liu, W.F.; Liang, J.K. Structural transition and atomic ordering in the non-stoichiometric double perovskite $\text{Sr}_2\text{Fe}_x\text{Mo}_{2-x}\text{O}_6$. *J. Alloys Compd.* **2003**, *353*, 42–47. [[CrossRef](#)]
44. Savinskaya, O.A.; Nemudry, A.P.; Nadeev, A.N.; Tsybulya, S.V. Synthesis and study of the thermal stability of $\text{SrFe}_{1-x}\text{M}_x\text{O}_{3-z}$ ($M = \text{Mo}, \text{W}$) perovskites. *Solid State Ion.* **2008**, *179*, 1076–1079. [[CrossRef](#)]
45. Merkulov, O.V.; Markov, A.A.; Naumovich, E.N.; Shalaeva, E.V.; Leonidov, I.A.; Patrakeev, M.V. Non-uniform electron conduction in weakly ordered $\text{SrFe}_{1-x}\text{Mo}_x\text{O}_{3-\delta}$. *Dalton Trans.* **2019**, *48*, 4530–4537. [[CrossRef](#)]
46. Hiroi, Z.; Hayamizu, H.; Yoshida, T.; Muraoka, Y.; Okamoto, Y.; Yamaura, J.; Ueda, Y. Spinodal decomposition in the TiO_2 - VO_2 system. *Chem. Mater.* **2013**, *25*, 2202–2210. [[CrossRef](#)]
47. Demond, A.; Sayers, R.; Tsiamtouri, M.A.; Romani, S.; Chater, P.A.; Niu, H.; Martí-Gastaldo, C.; Xu, Z.; Deng, Z.; Bréard, Y.; et al. Single sublattice endotaxial phase separation driven by charge frustration in a complex oxide. *J. Am. Chem. Soc.* **2013**, *135*, 10114–10123. [[CrossRef](#)]
48. Mikhailova, D.; Kuratieva, N.N.; Utsumi, Y.; Tsirlin, A.A.; Abakumov, A.M.; Schmidt, M.; Oswald, S.; Fuess, H.; Ehrenberg, H. Composition-dependent charge transfer and phase separation in the $\text{V}_{1-x}\text{Re}_x\text{O}_2$ solid solution. *Dalton Trans.* **2016**, *46*, 1606–1617. [[CrossRef](#)]

49. Smyth, D.M. The effect of dopants on the properties of metal oxides. *Solid State Ion.* **2000**, *129*, 5–12. [[CrossRef](#)]
50. Macías, J.; Yaremchenko, A.A.; Fagg, D.P.; Frade, J.R. Structural and defect chemistry guidelines for Sr(V,Nb)O₃-based SOFC anode materials. *Phys. Chem. Chem. Phys.* **2015**, *17*, 10749–10758. [[CrossRef](#)]
51. Adler, S.B. Chemical expansivity of electrochemical ceramics. *J. Am. Ceram. Soc.* **2001**, *84*, 2117–2119. [[CrossRef](#)]
52. Marrocchelli, D.; Perry, N.H.; Bishop, S.R. Understanding chemical expansion in perovskite-structured oxides. *Phys. Chem. Chem. Phys.* **2015**, *17*, 10028–10039. [[CrossRef](#)] [[PubMed](#)]
53. Sharp, J.H.; Brindley, G.W.; Narahari Achar, B.N. Numerical data for some commonly used solid state reaction equations. *J. Am. Ceram. Soc.* **1966**, *49*, 379–382. [[CrossRef](#)]